Materials Horizons

Silver-Purine MOFs for High-Performance Multi-Terminal Neuromorphic Memory

Journal:	*Materials Horizons*
Manuscript ID	MH-COM-10-2024-001425.R2
Article Type:	Communication
Date Submitted by the Author:	11-Dec-2024

Complete List of Authors:	Panda, Subhra; National Institute of Science Education and Research, School of Chemical Sciences Khator, Kanha; National Institute of Science Education and Research School of Physical Sciences, School of Physical Sciences Deswal, Priyanka ; IIT Delhi, Dept. Physics Nayak, Shashwat; National Institute of Science Education and Research School of Physical Sciences, School of Physical Sciences Pandey, Durgesh; IIT Delhi Patel, Suraj; National Institute of Science Education and Research School of Physical Sciences, School of Physical Sciences Agarwala, Suraj; NISER Ghosh, Dibyajyoti; Indian Institute of Technology Delhi, Chemistry Senanayak, Satyaprasad P; National Institute of Science Education and Research, Physics; University of Cambridge, Purohit, Chandra; National Institute of Science Education and Research, School of Chemical Sciences

New Concept:

Development of novel MOFs with reliable electrical and ionic conductivity is expected to open up myriad possibilities for a broad range of applications in optoelectronic devices, memory, and neuromorphic circuits. Majority of MOFs exhibit lower conductivity values of 10^{-10} S/cm which limits their applicability in devices. We utilize the concept of metal-metal bond (Ag-Ag in our case) to demonstrate conductivity values in the range of 10^{-4} S/m to 10^{-2} S/m. More interestingly, these solution processable MOFs demonstrate facile multi-channel pathway for controlled ionic movement and metal-metal bond for electronic conduction. Such a unique convergence of ionic and electronic conductivity allowed us to demonstrate high performance memory device where the states can be differentiated with a current distinction of up to 10^7 and a memory retention which can be extrapolated to 100's of years while operating at a low programming field of ~ 0.4 V/µm. Moreover, this unique MOF with mixed electronic and ionic transport can emulate multi-terminal complex neuronal response and demonstrate attributes of spike neural networks. Overall, our work provides conceptual advancements correlating the ionic and electronic conduction in MOF material obtained through a systematic chemical design that ultimately results in outstanding and unique brain-inspired device applications, which goes beyond conventional technologies envisaged for MOFs.

Data Availability Statement:

- The data supporting this article have been included as part of the Supplementary Information.

- Crystallographic data for $ACPPF_6$, $ACPSbF_6$, $MCPSbF_6$, and $MCPPF_6$ has been deposited at the CCDC under 2264862-2264865 and can be obtained free of charge from The Cambridge Crystallographic Data Centre via www.ccdc.cam.ac.uk/data_request/cif.

ARTICLE

Silver-Purine MOFs for High-Performance Multi-Terminal Neuromorphic Memory

Received 00th January 20xx,
Accepted 00th January 20xx

DOI: 10.1039/x0xx00000x

Subhra Jyoti Panda[a], Kanha Ram Khator[b], Priyanka Deswal[c], Shashwat Nayak[b], Durgesh Pandey[d], Suraj K. Patel[b], Suraj Kumar Agrawalla[a], Dibyajyoti Ghosh[c,e],* Satyaprasad P. Senanayak[b,f],* Chandra Shekhar Purohit[a,f]*

Neuromorphic and fully analog in-memory computations are promising for handling vast amounts of data with minimal energy consumption. We have synthesized and studied a series of homo-bimetallic silver purine MOFs (1D and 2D) having direct metal-metal bonding. The N7-derivatized purine ligands are designed to form bi-metallic complexes under ambient conditions, extending to a 1D or 2D metal-organic framework. Owing to the unique structural property, these complexes exhibit voltage-controlled tunable ionic conductivity, thereby allowing us to demonstrate two-terminal non-volatile memory characteristics with a retention time of more than 10^4 seconds, an I_{LRS}/I_{HRS} ratio of 10^7, along with volatile memory functionality. The atomistic computations corroborate the dominant influence of the organic framework on controlling ionic diffusion through porous channels. Finally, this capability to tune the ionic conduction in these MOFs was utilized to emulate synaptic plasticity, such as long-term potentiation/ depression (LTP/LTD) and complex multi-terminal heterosynaptic plasticity. Attributes of spiking neural networks (SNNs) such as spike time-dependent plasticity (STDP) featuring a unique symmetric anti-Hebbian learning with an impressive STDP ratio of 109, and paired-pulse facilitation (PPF) index of 60 were recorded, which is among the best for MOF based neuromorphic devices. Overall, our technique of designing novel metal-organic frameworks with facile porous channels for controlled ionic motion could pave the way for a novel class of materials, allowing seamless integration for bio-synaptic electronic devices.

Introduction

In this era of the Internet of Things (IoT) and artificial intelligence (AI), there is a ubiquitous need for powerful and efficient computing systems.[1] Conventional computation faces two major challenges: the von Neumann bottleneck and the saturation of Moore's Law in the quantum limit.[2-4] To address these challenges, neuromorphic computing, and fully analog in-memory computation are conceptualized as a way forward for processing vast amounts of data with minimal time and energy consumption.[5-7] Significant advancements have been made in creating neuromorphic devices such as afferent nerves,[8, 9] optoelectronic sensors,[10-12] olfactory neurons,[13] adaptive biosensors,[14] optomemristors,[15] and neuromorphic displays.[16] Similarly, extensive research on non-volatile resistive memory devices has been carried out with covalent-organic/metal-organic materials having two or multiple stable resistance states, which can be controlled by electrical/optical simulation, making them well-suited for storing information.[17-24] Notably, most of these neuromorphic devices emulate bio-inspired learning processes through mechanisms such as electroforming, variation of the Schottky barrier, etc., which are different from the ionic-based mechanism found in biological learning and synaptic processes.[25] Hence, obtaining the full potential of a neuromorphic device necessitates a learning mechanism using ionic channels similar to the synaptic response.[3]

Among various materials explored for such applications, MOFs with ionic and electronic conductivity have evolved as an attractive alternative material with reported applications in electrochromic, neuromorphic, and energy storage devices.[26] MOFs are crystalline, porous, and rigid molecular networks where the metal atom, organic framework, and ionic components can provide varied pathways for conduction. Generally, MOFs are bad conductors of electricity, with conductivities of ~10^{-10} S/cm.[27, 28] Various methods have been devised to enhance both electronic and ionic conductivity in MOFs, such as voltage-induced filament formation,[29, 30] H-bonding interaction,[31, 32] charge transfer interaction,[24] and proton conduction.[33] We expected that the "through bond" conductivity may be enhanced by incorporating direct metal-metal (MM) bonding in MOFs. Although synthesizing long 1D, 2D, and 3D arrays of connected MM-linked coordination complexes or polymers remains challenging for synthetic chemists, a limited number of discrete complexes with a finite number of linear MM bonds are reported.[34-41] When metal atoms are in bonding distance, their electrical properties rely on the extent of electron delocalization. Improving the charge delocalization enhances the electrical

[a] School of Chemical Sciences, National Institute of Science Education and Research (NISER), An OCC of HBNI, Bhubaneswar, 752050, Odisha, India.
[b] Nanoelectronic and Device Physics Lab, School of Physical Sciences, National Institute of Science Education and Research (NISER), An OCC of HBNI, Bhubaneswar, 752050, Odisha, India.
[c] Department of Physics, Indian Institute of Technology, Delhi, Hauz Khas, New Delhi 110016, India.
[d] Department of Chemistry, Indian Institute of Technology, Delhi, Hauz Khas, New Delhi 110016, India.
[e] Department of Materials Science and Engineering Indian Institute of Technology, Delhi, Hauz Khas, New Delhi 110016, India.
[f] Center for Interdisciplinary Sciences (CIS), National Institute of Science Education and Research (NISER), Bhubaneswar, Jatni, Khurda, Odisha 752050, India
Supplementary Information available: [details of any supplementary information available should be included here]. See DOI: 10.1039/x0xx00000x

conductivity,[42] making them suitable for novel nanoelectronics devices.[43] Therefore, designing and synthesizing solution-processable MOFs with discrete units containing MM bonds connected by organic spacers is imperative to design better conductors. Due to the presence of both direct MM bonds and ionic moieties, such as counter anions in the lattice, these materials are expected to exhibit better ionic and electronic conductivity. A recent study demonstrated promising control of the electrical conductivity of a polymeric material with a direct Cu-Cu bond.[44] However, to the best of our knowledge, there is no report on MOFs incorporating bi-metallic complexes with direct metal-metal (MM) bonds, serving a similar purpose for nano-electronic devices.

Herein, we describe the synthesis, characterization, and electrical behavior of four solution-processable Ag(I)-purine MOFs. These purine derivatives are intended to form bi-metallic coordinate complexes in which two metal centers are close enough to have MM bond and act as a spacer. Thereby, an array of connected bimetallic centers in a polymeric network is created, exhibiting both electronic and ionic conductivity. The impact of the metal-organic framework on tuning the ionic transport in these MOFs are studied with atomistic details using computational simulations. Furthermore, from quantum mechanical calculations, we observed that the entropic disorder of the ions substantially modifies the electronic conduction in these frameworks, which is consistent with the experimental measurements. Leveraging the fine tunability of ionic conductivity in these molecules under bias, we demonstrate two-terminal non-volatile memory characteristics with a significantly high I_{LRS}/I_{HRS} ratio of 10^7 and a retention time exceeding 10^4 seconds, which extrapolates to 100 years. Remarkably, these devices operate at an ultra-low electric field of 0.1-1 V/µm and consume energy in the order of nano Joule. Beyond their memory potential, $MCPSbF_6$ exhibit neuronal properties such as long-term potentiation (LTP), long-term depression (LTD), and paired-pulse facilitation (PPF) and Spike Time Dependent Plasticity (STDP) with a symmetric anti-Hebbian learning process, indicating the efficacy of such mixed conducting MOF structures for neuromorphic applications.[45, 46]

In addition to these conventional learning behaviors, we demonstrate six-terminal neuromorphic devices from $MCPSbF_6$, which exhibit heterosynaptic neural computing that is generally not achievable with two-terminal memristors.[3] Notably, the learning mechanism in these devices is based on the modulation of electrical and /or ionic conductivity through chemically designed porous ionic channels analogous to the mechanism of conduction observed with biological synapses.

Results and Discussion:

Nucleobases are well-investigated for the construction of 2D and 3D metal-organic frameworks.[47-49] However, only a few reports exist in the literature where MM bonds are present.[50-53] Moreover, most MOF material cannot be processed in solution due to the requirement of adverse processing conditions such as higher than room temperature processing, strongly acidic or basic conditions, and insolubility in common solvents.[54] We envisage the formation of a system by alkylating N7 to produce a ligand that can coordinate multiple metal ions, overcoming the above-mentioned limitations. Two N7 derivatives of 6-chloropurine, namely N7-allyl-6-chloropurine (ACP) and N7-methyl-6-chloropurine (MCP), were prepared following a literature report (**SI section 2.1-2.2**).[55] These derivatives are soluble in organic solvents and readily form MOFs upon the addition of silver salt(s). To investigate the metal binding behavior, these were further crystallized with two silver salts ($AgSbF_6$, $AgPF_6$). The choice of silver salt is based on the fact that silver(I), being a soft cation, coordinates well even with electron-deficient nitrogen-containing heterocycles, such as pyrazine,[56] and purine nucleobases to form 2D/3D MOFs.[57, 58] The anions are chosen to be non-coordinating so that they are freely available in the lattice and may contribute to ionic conductivity when biased with an electric field. Thus, four complexes of silver, two with ACP ($ACPSbF_6$, $ACPPF_6$) and two with MCP ($MCPSbF_6$, $MCPPF_6$), were synthesized, and a detailed understanding of the structure-property correlation is developed. These complexes were characterized by NMR spectroscopy (**SI section 2.3-2.10**). Crystal structures of these complexes reveal that even if the molecular network for conduction alters due to the variation of the alky group attaching to N7 or counter anions, a bi-metallic complex is always formed with Ag^+ ions (allyl in **Figure 1,** methyl **in Figure 2**) coordinating to N3 and N9. The other nitrogen (N1) extends the coordination, forming 1D and 2D coordination polymers.

The single crystals of $ACPSbF_6$ were obtained from a dilute methanol solution by slow evaporation. Solid-state analysis demonstrates $ACPSbF_6$ forms an unusual three-blade paddle wheel structure around a bi-silver metal core. It may be noted that although paddle wheel structure is known for Cu, Rh, Mo, Re, Cr, etc., but no such compound for Ag(I) has been reported to date to the best of our knowledge.[51, 59] The Ag-Ag distance is 3.00(8) Å, slightly longer than the Ag-Ag bond distance of 2.88(9) Å in metallic silver.[60] Note that the geometries around the two silver ions are different (**Figure 1c**). The coordination around Ag1 can most appropriately be described as a trigonal pyramidal geometry. Three N3 from three ACP ligands occupy the corners of the trigonal base with Ag-N3 bond distances 2.23 Å, 2.23(7) Å, 2.27(5) Å, and Ag2 occupying the apex. Ag2 forms a distorted trigonal bipyramidal geometry with three N9 [2.27(8) Å, 2.32(8) Å, 2.36(2) Å] forming the trigonal base, Ag1 at one apex and N1 atom at another.[61] This N1 connects two units, resulting in the linear polymer of the paddle wheel units, and the charge is balanced by SbF_6^- anions present in the lattice. We optimized the ground-state MOF geometries to further validate our experimental observations using density functional theory (DFT) based on atomistic simulations. As included in the SI (**Figure S33** details in a later section), the optimized geometries retain the overall framework connectivity with minimal distortion, supporting the experimental stability of the MOF structures.

The morphological characteristics of $ACPSbF_6$ and $ACPPF_6$ were examined using scanning electron microscopy (SEM) and transmission electron microscopy (TEM). SEM imaging revealed a distinct spherical morphology for both materials (**Figure 1f, 1g**). The average particle sizes of $ACPSbF_6$ and $ACPPF_6$ were determined to be (3.5 ± 0.9) µm and (2.1 ± 0.4) µm, respectively. To further elucidate the effect of concentration on the film morphology behavior, images of the thin films of both MOFs were acquired under both dilute (single 10 µL drop cast of 3 mg/mL solution) and concentrated conditions (multiple drop cast of 5.5 mg/mL solution). Morphological investigation clearly depicts that under dilute conditions, the spherical particles were well-dispersed, while concentrated deposition resulted in the aggregation and stacking of the spheres. TEM analysis corroborated the spherical morphology of both MOFs, providing additional insights into their structural characteristics (**Figure S23a, S23c**).

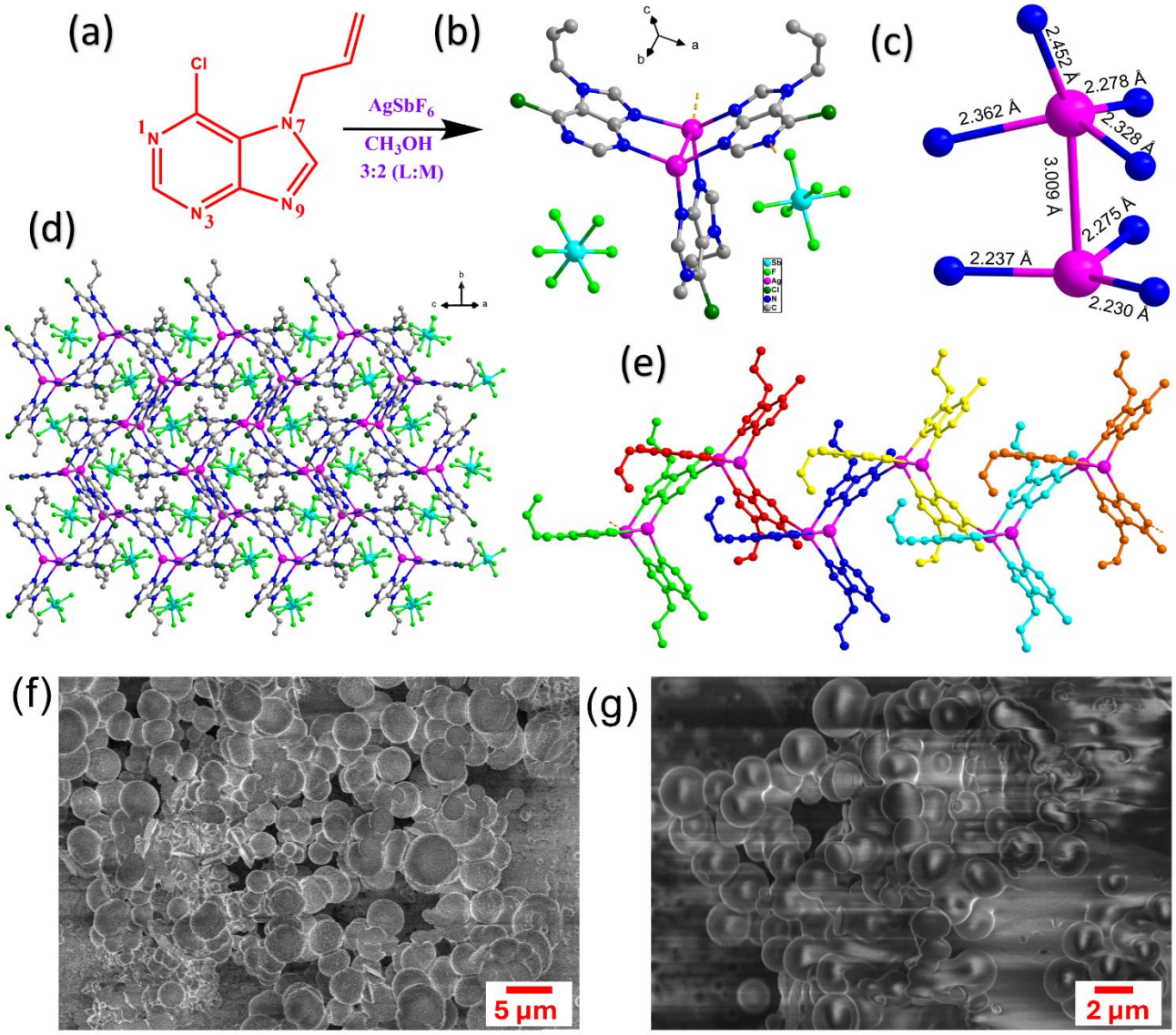

Figure 1. Synthesis of $ACPSbF_6$ and its crystal structure. a) ACP ligand and synthetic scheme. b) asymmetric unit of the $ACPSbF_6$ complex, a three-blade paddle wheel unit with Ag-Ag core and two SbF_6^- anions. c) geometry and bond distances in $ACPSbF_6$ (Ag in pink, N in blue). d) crystal packing diagram showing Metal-organic frameworks and anions reside in the void. e) linear array of paddle wheel units, (1D MOF) different units are shown in different colors. Hydrogen atoms are omitted for clarity; f) Scanning electron microscopy (SEM) image of f) $ACPSbF_6$, g) $ACPPF_6$ along with the scale bars.

NMR spectroscopy was employed to elucidate the kinetic profile of $ACPSbF_6$ complex formation. To avoid rapid complexation, we have used 15 mM solutions (in CD_3OD) of both the ligand and salt for this experiment (**Figure S5b**). Two singlets at 8.79 and 8.69 ppm in the ^1H NMR spectrum of ACP ligand correspond to aromatic H2 and H8, respectively. Upon adding an equivalent amount of $AgSbF_6$ to the NMR tube, two new peaks at 9.06 and 9.05 ppm appeared after 4 minutes, indicating the formation of a complex ($ACPSbF_6$). Further, the peaks corresponding to the ligand shifted to 8.88 and 8.80 ppm, possibly due to the change in the ionic strength of the solution, which disappeared in 25 minutes, indicating the complete formation of the complex.

The phase purity of bulk material was verified using Powder X-ray diffraction (PXRD) analysis. The obtained powder diffraction pattern perfectly matched the simulated single-crystal pattern, as depicted in **Figure S6,** confirming the phase similarity of the bulk materials and single crystal.

The complexation of $MCPSbF_6$ and solid state analysis is shown in **Figure 2**. To study the solid-state structure of $MCPSbF_6$, suitable crystals for X-ray diffraction studies were obtained from a dilute methanolic solution by slow evaporation. The asymmetric unit of $MCPSbF_6$ exhibits a dimeric unit where each MCP ligand is coordinated to two silver atoms via the N3 and N9 atoms. These dimeric units further connect to each other through the N1 atom, forming an octa-silver square-like repeating unit (**Figure 2b**). These square units repeat themselves, creating a 2D sheet that extends throughout the crystal lattice (**Figure 2c**). As shown in **Figure 2d**, the SbF_6^- anions are located above and below the square voids in the metal-organic framework. Consequently, two layers of anions exist between each layer of cationic MOF, creating an ion channel. Screening of these anions in the channel, when an electric potential

is applied, contributes to the ability of the material to exhibit memory and neuromorphic behavior. Each silver is coordinated with N3, N9, and N1 of MCP and another silver to form highly distorted tetrahedral geometry. The Ag-Ag bond distance is 2.99(6) Å (**Figure 2e**), similar to $ACPSbF_6$.

Interestingly, morphological characteristics of $MCPSbF_6$ and $MCPPF_6$ revealed a rectangular plate-like morphology for both materials at higher concentrations (**Figure 2f, S21 and S22**), whereas at lower concentrations, both MOFs exhibited a spherical morphology, attributed to limited nucleation and growth analogous to the previously studied MOFs (**Figure S22c, S22d**). This spherical morphology was further confirmed through high-resolution transmission electron microscopy (HR-TEM). HR-TEM images of $MCPSbF_6$ and $MCPPF_6$ are shown in **Figures S23b and S23d**. **Figure 2g** presents the lattice fringes of MCPSbF6, with **Figure 2h** showcasing magnified fringes displaying a width of 0.218 nm. **Figure 2i** depicts the plane intersecting the Ag-Ag bond, demonstrating a distance of 0.2186 nm, which aligns precisely with the fringe width observed in the HR-TEM image. For this measurement relatively lower concentration has been used to ensure distinct well separated

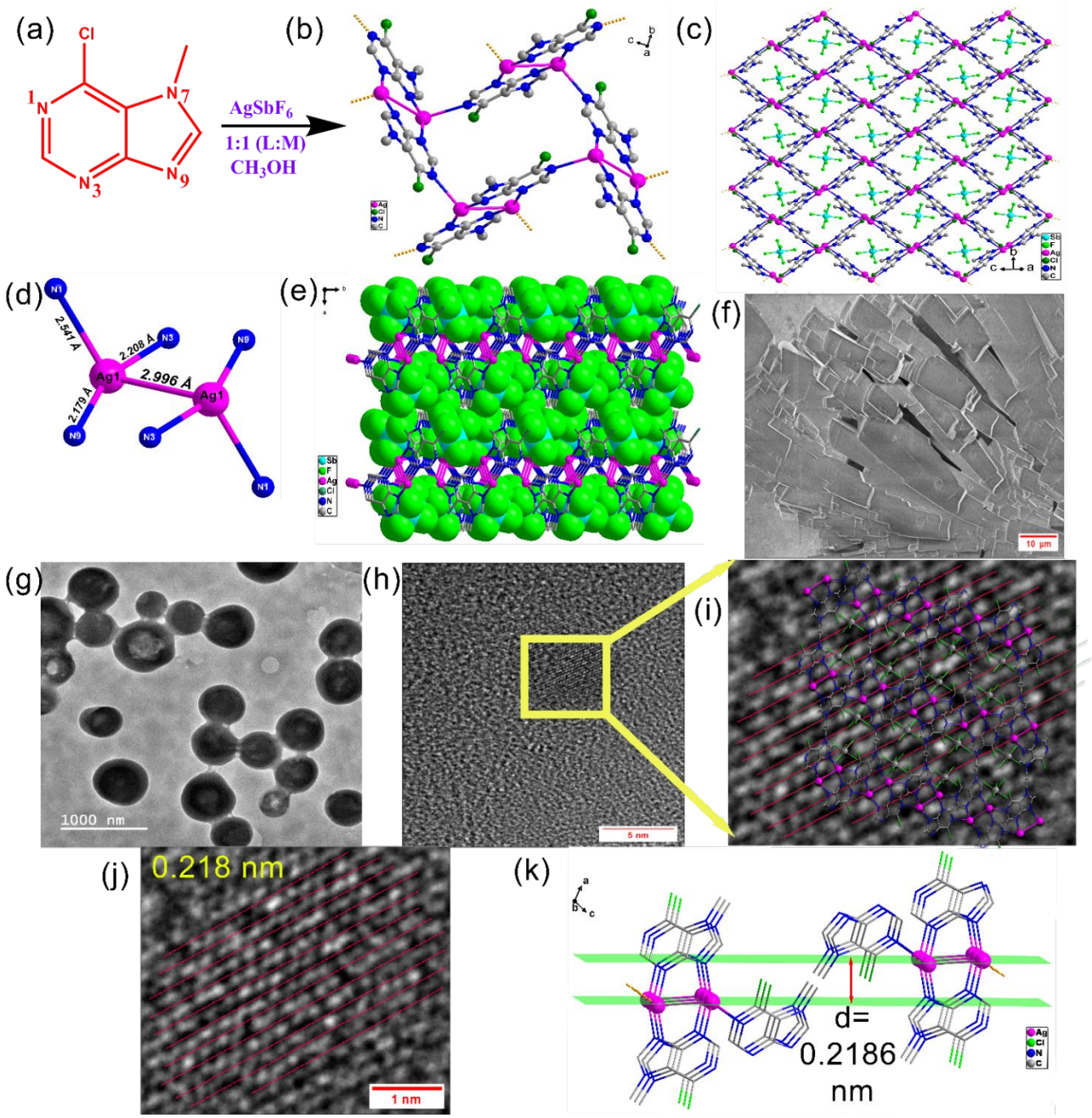

Figure 2. Synthesis of $MCPSbF_6$ and its crystal structure. a) MCP ligand and complex synthesis. b) crystal structure of the $MCPSbF_6$ complex. The repeating unit consists of an octa-silver square. c) 2D sheet of octa-silver square MOF, SbF_6^- anions are in the lattice channel. d) crystal packing along the z-axis showing the MOF and anions present above and below the 2D sheet (SbF_6^- anions are in space fill model). e) geometry and bond distances around Ag ion (Ag in pink, N in blue). Hydrogen atoms are omitted for clarity; f) Scanning electron microscopy (SEM) image of $MCPSbF_6$; g) TEM image of $MCPSbF_6$ showing lattice Fringe width; h) Zoomed fringe width of distance 0.22 nm and $MCPSbF_6$ stacked on top; i) Lattice plane passing through Ag-Ag bond with the distance of 0.2186 nm.

aggregates which allow appropriate visualization of the structural attributes.

The formation kinetics of the complex was studied using ^{1}H NMR spectroscopy. MCP's H2 and H8 peaks were observed at 8.75 ppm and 8.59 ppm, respectively. The addition of $AgSbF_6$ solution (in CD_3OD) resulted in the appearance of two new peaks at 9.05 ppm and 9 ppm, indicating the formation of the product $MCPSbF_6$. No peaks corresponding to free ligands were found in the spectra, like in the previous case (**Figure S14)**. This suggests that the rate of formation of $MCPSbF_6$ is faster than $ACPSbF_6$. To verify the bulk purity of $MCPSbF_6$, a powder X-ray diffraction (PXRD) experiment was performed. Nevertheless, similar to the earlier case, the obtained PXRD peaks exhibited a complete correspondence with the simulated single-crystal pattern, as illustrated in **Figure S15,** indicating the phase similarity/purity of the bulk thin films and single-crystal material. Understanding the inherent photo-induced instability of Ag complexes, we intended to characterize the photostability of the complexes by exposing the samples to white light (14 W and 1400 lm) for 16 hours (setup in **SI section 1.3**). PXRD data were collected before and after exposure. Surprisingly, even after light exposure for 16 hours, no change is observed in the PXRD pattern, indicating that both complexes are stable to visible light (**Figure S8, S16**).

With these well-characterized complexes in hand, we then explored the electrical properties of these bimetallic MOFs using two terminal lateral devices consisting of Cr/Au electrodes (L = 100 µm, W = 1 mm). Lateral devices were fabricated by drop-casting 100 µL of the respective methanol solutions (Concentration 11.5 mM – 20 mM) (schematic **Figure S24**). Two methods were employed to optimize the film: (a) drying the films at room temperature under dark conditions and (b) annealing the films at 80 ˚C for 15 minutes in the dark to obtain the films. Upon measurement of I-V characteristics at room temperature, we observe that annealing of the films reduced the channel current by at least two orders of magnitude compared to the films dried at room temperature (**Figure S25a**). Encouraged by the excellent device performance, we also fabricated and tested flexible devices on PET substrates (**Figure S25b**). Surprisingly, the performance of these flexible devices was comparable to those with glass substrates, indicating the possibility of designing flexible electronic applications using these materials.

Nevertheless, we followed the first fabrication method (involving film formation at room temperature) for estimating the electronic and ionic conductivity (**Figure 3**) of all the bimetallic MOF materials. The I-V characteristics of these optimized films at room temperature are shown in **Figure 3a**. All the devices exhibit significant clockwise hysteresis with the channel current value lower in the reverse scan, indicating ionic screening of the potential due to ion migration under bias. In the forward voltage sweep (0→80V), negative ions accumulate near the anode, creating an electric field opposite to the applied electric field. Thus, the observed current in the reverse voltage sweep (80 V→0 V) is lower, which results in a lower channel current (Schematic in **Figure 3d**). The screening effect also results in negative differential resistance (NDR), which is prominent at lower scan rates only because slow-moving anionic species get enough time to screen the applied field efficiently. Thus, the channel current decreases upon increasing the bias, and we observe a non-ohmic NDR regime. Since anionic species are the migrating species in our material, we observe NDR in the positive cycle of bias only. Nevertheless, the observation of NDR in the I-V characteristics inspired us to utilize these devices for diverse neuromorphic applications.[62] We observe that the channel current of MCP-based MOFs is higher than ACP-based MOFs by at least two orders of magnitude. This may be attributed to the 2D molecular arrangement observed in the crystal structure of MCP-based polymers compared to the 1D molecular arrangement in the ACP MOFs.[5, 7, 63] Also, MCP-MOFs have ~45% higher Ag^+ and anion density (SI **section 2.13**). To further verify the ionic contribution to the overall conductivity, we measured I-V characteristics while varying the scan rate (10 V/s to 500 V/s). Details of the scanning rate measurement are provided in **Section 4** of Supporting Information. It was observed that the channel current decreases as the scan rate decreases, indicating that at lower scan rates, more ions are migrating in the channel.[63, 64] They have sufficient time to attain an equilibrium position in reaction to the applied electric field, thereby increasing the screening effect (**Figure 3b** and **S26**). Notably, we observe that the hysteresis variation with scan rate is significantly higher in the positive voltage regime in comparison to the measurement in the negative voltage regime, indicating that anionic species (PF_6^- or SbF_6^-) which are free to move relative to the cationic species (MOF in this case), are possibly the major contributor to the hysteresis in these I-V characteristics.[65, 66] Nevertheless, it is noteworthy that the conductivity studies implement voltages ranging from 40 V to 100 V, translating to an effective electric field of 0.4V/µm to 1V/µm, which is significantly lower than most similar reports (Compared in **Table S4**). While these higher voltages are necessitated by the relatively long channel length, we have confirmed that reducing the channel length while maintaining the same electric field yields currents of similar magnitude (as shown in **Figure S27**). This demonstrates that the memory devices can be operated at much lower voltages without sacrificing the device's performance, and the channel length is just a scaling factor.

To further confirm the contribution of anionic species to the overall conduction, we substituted these non-coordinating fluorinated anions (SbF_6^-, PF_6^-) with coordinated NO_3^- ions. This is achieved by using a MOF derived from $AgNO_3$ salt with MCP as the ligand. In $MCPNO_3$, the oxygen atom of nitrate anion coordinates with the Ag^+ ion ($d_{Ag\text{-}O}$ is 2.56(9)Å, $d_{Ag\text{-}Ag}$ is 3.08(7) Å) (**Figure S20**). We observe a significant decrease in channel current by at least 2 orders of magnitude due to the substitution of nitrate anions. Correspondingly, the ionic conductivity decreases from 4.8×10^{-2} S/m to 1×10^{-4} S/m (discussed in the later section), clearly pointing to the overall contribution of free non-coordinating anionic species to the ionic conductivity of the MOFs. We define the screening factor ($\chi = I_{500V/s} / I_{10\ V/s}$) as the ratio of channel current measured at a particular voltage while the scan rate is changed from 500 V/s to 10 V/s (**Figure S26**). The screening factor $\chi \sim 1.5$ is obtained in the negative voltage regime, which increases to $\chi \sim 4$ in the positive voltage regime, reiterating the dominant contribution of the anionic species in the hysteretic characteristics of these devices (**Figure 3b** and **S26**). Furthermore, we observe that, when the I-V characterization is performed under vacuum, the channel current decreases by at least three orders of magnitude (1 µA to 1 nA in $MCPSbF_6$), indicating that vacuum-based removal of trapped solvent possibly mediates the ionic conductivity in these materials (**Figure S28**). To illustrate that this hysteretic characteristic can be modified in a controlled manner for practical device application, we performed I-V characteristic measurements while modifying the bias voltage. The area under the hysteresis scales linearly with the voltage range of the measurement (**Figure 3c** & **Figure S29**), effectively indicating enhanced ion migration.

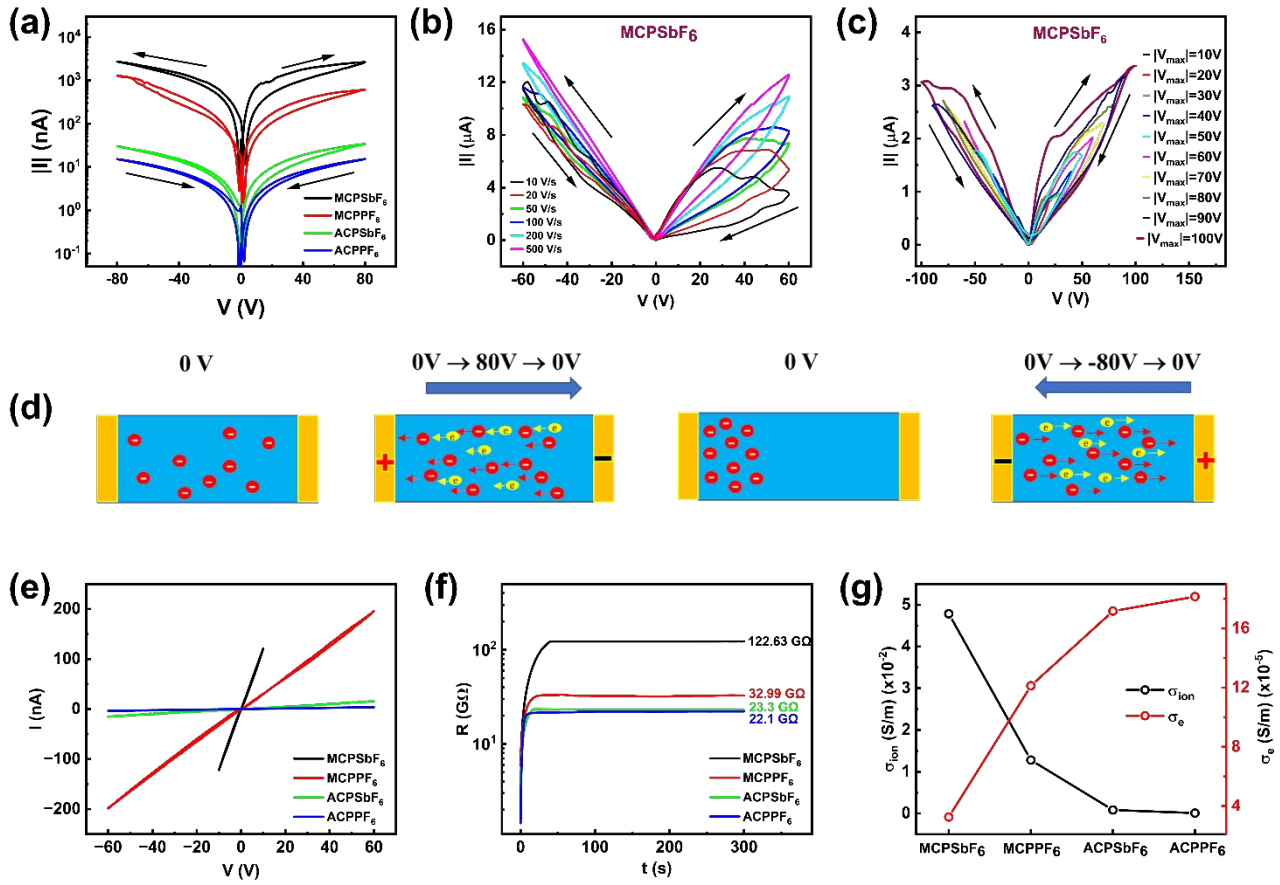

Figure 3. a) Comparison of the I-V characteristics of $MCPSbF_6$, $MCPPF_6$, $ACPSbF_6$, and $ACPPF_6$. I-V characteristics of $MCPSbF_6$ measured at b) different scan rates (4 V/s to 500 V/s). c) by increasing the voltage range from ±10 V to ±100 V at a step size of 10 V. Note that the arrows show the direction of hysteresis in all the plots. d) A schematic diagram of the device showing the ionic movements in different regimes of I-V sweep. The blue arrow represents the direction of the electric field between the two electrodes. e) Hysteresis-free I-V characteristics of the molecules at 10000 V/s scan rate used to calculate the combined electronic and ionic conductivity. f) Time evolution of resistance of the molecules, measured while applying a constant current of 2 nA. g) Comparison of the electronic and ionic conductivity of the various MOF complexes.

All the above measurements indicate that anions in these metallopolymers significantly contribute to the hysteretic characteristics and screening behavior, creating non-idealities in the I-V characteristics, thereby making it difficult to estimate and isolate the electronic and ionic contribution to the overall conductivity. We thus performed an I-V characteristics measurement at 10,000 V/s to obtain near-ideal linear I-V characteristics without any hysteresis (**Figure 3e**), such that Ohms law can be utilized for estimating the conductivity. The I-V characteristics of $MCPSbF_6$ exhibited hysteresis even at a high scan rate of 10000 V/s when the voltage range is ±60 V. Hence, to ensure hysteresis-free I-V characteristics, the measurement was restricted only to a voltage range of ±10 V. A comparison between the I-V measurement at different voltage ranges for $MCPSbF_6$ is shown in **Figure S30a**. Nevertheless, the conductivity obtained from these hysteresis-free characteristics has the combined contribution of electronic and ionic conductivity (σ_{total}).[67, 68] To determine the electronic conductivity, we performed a galvanostatic measurement wherein a constant current was applied, and the R(t) variation was monitored. When a constant current is applied, ions start screening the current flow, causing the resistance to increase until resistance saturation is observed. In this saturation regime, the resistance is solely contributed by electronic conduction (σ_{ele}).[68] Galvanostatic measurements were performed with constant current values ranging from 20 pA to 2 nA. We observe that at lower current values, the saturation regime was not obtained until 300 seconds (for example, see **Figure S30b**), and therefore, a suitable value of current was chosen for each molecule for which a saturation regime was achieved. A time limit of 300 seconds was chosen to achieve saturation in order to ensure that devices are not under current stress for a prolonged time. The galvanostatic measurements for the four MOF complexes are shown in **Figure 3f,** where a constant current of 2 nA was utilized. By subtracting the σ_{ele} from the σ_{total}, we estimated that $MCPSbF_6$ has the highest ionic conductivity, reaching up to 4.8 x 10^{-2} $S.m^{-1}$, followed by $MCPPF_6$, $ACPSbF_6$, and $ACPPF_6$, (**Table S3** & **Figure 3g**). This trend can be correlated to the higher anion concentration and dimensionality of the MOFs. The enhanced conductivity of the 2D MOF (MCP-based) thin films, as observed in the SEM images (**Figures 1, 2, S21, and S22**), can be attributed to the formation of larger, interconnected rectangular plates. This extended 2D-nanostructures structure provides a more continuous pathway for ion transport, facilitating efficient transport compared to the 1D MOF (ACP-based) counterparts. The effect of dimensionality on the conductivity is evident from the SEM images (**Figure 1, Figure 2, Figure S21** and **S22**), the formation of larger grains in size and spanning the space with continuous grain formation in thin film of 2D MOFs (MCP based), facilitates the movements of ions more efficiently than their 1D counterparts(ACP based). In order to highlight the contribution of the M-M bond, we also performed measurements with two additional MOFs: ZnMCPCl and HgMCPCl.[69] ZnMCPCl is a discrete

complex without any M-M bond, and consequently, we observe that the conductivity falls down to a value of 1.8×10^{-4} S/m. In contrast, the Hg counterpart exhibits slightly lower conductivity compared to other Ag-complexes owing to the presence of the weak M-M bond and coordinated Cl^- anion. Detailed discussion to obtain a microscopic understanding of the observed conductivity trends for various control samples is provided in **SI section 8**.

Interestingly, the electronic conductivity trend was observed to be the exact opposite of the ionic conductivity trend. However, the maximum electronic conductivity was estimated to be only 1.8×10^{-4} $S.m^{-1}$($MCPPF_6$), which is lower than the lowest ionic conductivity of 6.6×10^{-4} $S.m^{-1}$ observed for $ACPPF_6$ (among the four primary MOFs). Based on a simple volumetric estimation to obtain the ionic concentration, the ionic mobility was estimated to be in the range of 2.5×10^{-4} $cm^2V^{-1}s^{-1}$ for $MCPSbF_6$, which decreases to ~ 6×10^{-6} $cm^2V^{-1}s^{-1}$ for $ACPPF_6$ consistent with the variation of charge transport in 2D crystal versus 1D crystal. Notably, the ionic mobility of SbF_6^- based metallopolymers was higher than PF_6^- based molecules. This behavior is associated with the enhanced crystallinity of the SbF_6^- containing bimetallic MOFs, which corresponds to a decrease in FWHM or enhanced crystallinity of SbF_6^- in comparison to the PF_6^- based molecules (**Figure S14, S18**). Nevertheless, all these measurements clearly conclude that the conductivity in these MOFs results from a combination of factors originating from the dimensionality of the network, the existence of the M-M bonds, and the extent of coordination with the anion and intrinsic crystallinity of the samples.

To obtain a molecular understanding of the ion conduction trend in these MOFs, we computationally model the vacancy-assisted PF_6^-/SbF_6^- ion migration process in $MCPPF_6$ and $MCPSbF_6$ (see details of the computational methodology in **SI section S9**). Our initial goal is to understand the influence of the migrating anion on the overall ionic conductivity in these MOFs (see structural details in **SI section S10**).[70] The computations, using nudged elastic band (NEB) methods,[71] reveal that the migration barriers for PF_6^- and SbF_6^- ion hopping are 0.62 eV and 0.56 eV, respectively, as depicted in **Figure 4a**. which matches with our experimental trends of ionic conductivity plotted in **Figure 3g.** To understand the atomistic reason behind such a trend of anionic species migrations in MCP-based MOFs, we investigate the local structural distortions during the ion diffusion.

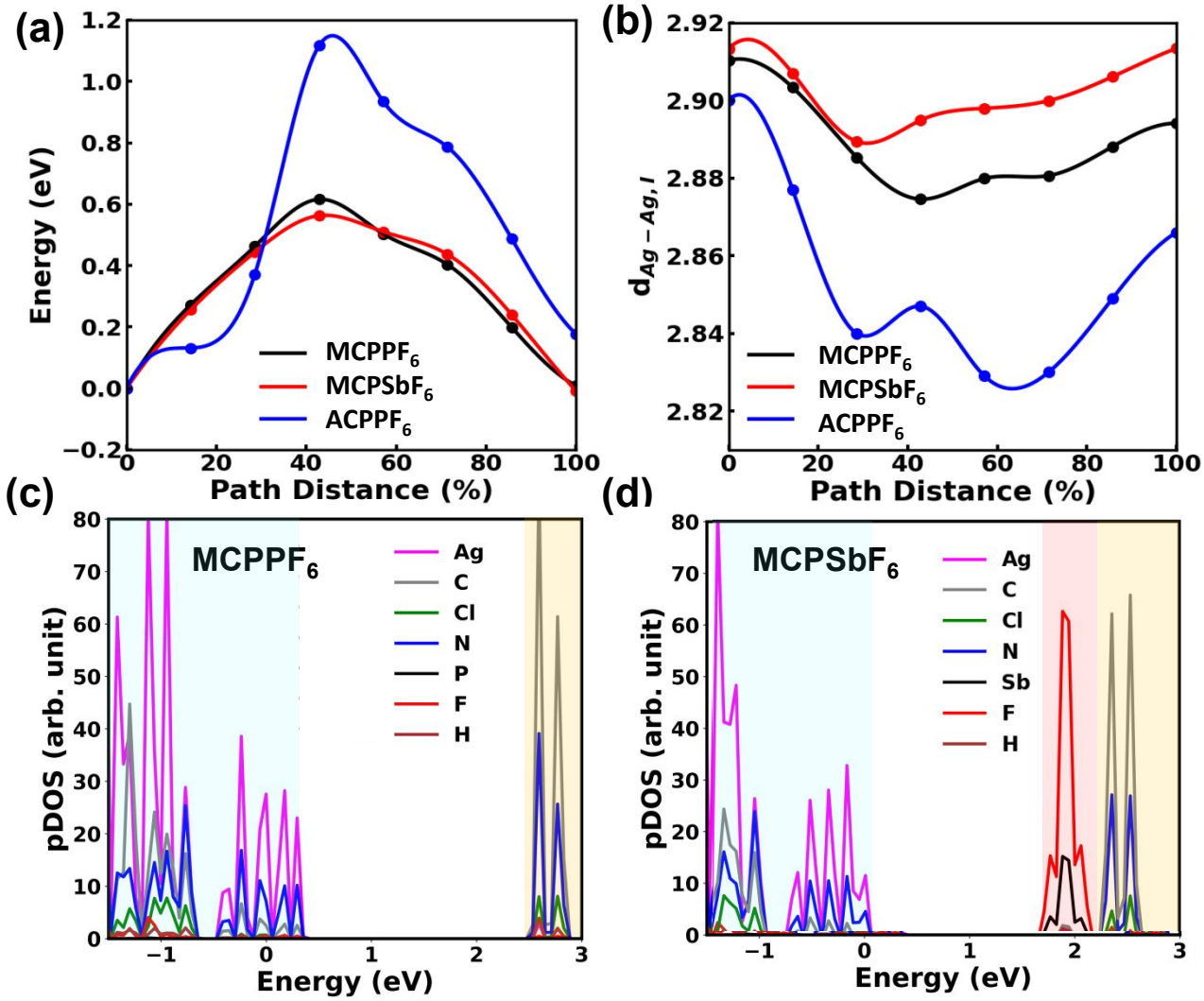

Figure 4: a) Energy profiles illustrating XF_6^- (X = Sb/P) ion migration in $MCPPF_6$, $MCPSbF_6$, and $ACPPF_6$. b) The distance between Ag ions in proximity to the initial position of the migrating XF_6^- ion (X = Sb/P; $d_{Ag\text{-}Ag,I}$). Partial density of states (PDOS) for c) $MCPPF_6$ and d) $MCPSbF_6$, showing the valence band, molecular state region, and conduction band shaded in blue, red, and yellow, respectively.

The local structural distortions during ion diffusion are tracked from the difference between the Ag-Ag metal bond distance ($d_{(Ag-Ag)}$) values: (1) the Ag-Ag bond distance in proximity to the initial position of migrating XF_6^- ion (X = Sb/P; $d_{Ag-Ag,I}$) (**Figure 4b**), and (2) the Ag-Ag bond distance near the final position of migrating XF_6^- ion ($d_{Ag-Ag,F}$) (**Figure S34a**). A schematic illustrating these two structural parameters is included in **Figure S34b**, and the ion migration pathways are shown in **Figure S34c-S34e**. The plotted d_{Ag-Ag} values in **Figure 4b** depict that the Ag-Ag bonds undergo greater elongation along the Minimum Energy Pathways (MEPs) during PF_6^- ion hopping. Importantly, this elongation persists, and the bonds cannot return to their initial positions, resulting in a strained configuration. This sustained strain contributes significantly to the concurrent structural modifications in the local geometry of the framework. Such local structural modification partially increases the migration barrier for PF_6^- through the MCP channel. In contrast, for SbF_6^-, the d_{Ag-Ag} bonds get marginally elongated, indicating stronger electrostatic interactions between Ag^+ and SbF_6^- ion bonds, thereby reducing the migration barrier for SbF_6 diffusion in MCP-based MOF.

Next, in order to understand the role of the metal-organic framework on ion migration, we calculate the MEP and associated migration barrier for PF_6^- anion diffusion in $ACPPF_6$. The migration barrier for PF_6^- ion hopping in ACP-based MOF is 1.1eV (**Figure 4a**). Tracking the local structural modifications along MEP, we find much more elongated d_{Ag-Ag} bonds in $ACPPF_6$ (**Figure 4b**). Such distortion sustains higher strain, preventing the bonds from returning to their initial positions. Overall, these simulations emphasize that local structural distortions substantially impact the anion migration through MOF channels, ultimately controlling the overall ionic conductivity of these materials. The more the elongation of d_{Ag-Ag} bonds during anion transport, the higher the associated migration energy barrier. Furthermore, atomistic simulations suggest that the porous channels are filled with negatively charged SbF_6^- or PF_6^- ions. These anions interact with the positively charged framework, with Ag sites acting as charge centers. As the non-coordinating anions are not chemically bonded with the framework, they can migrate through the porous channels by following a sequential hopping mechanism, as modeled, through CI-NEB-based simulations. On the contrary, Ag^+ ions form stable coordination bonds with MCP ligands, creating a rigid MOF framework. Thus, migration of those cations is highly unlikely due to the associated substantially large migration energy. Such Ag^+ migration could potentially disrupt the framework and substantially damage the material. However, our MOF remained stable throughout all the experiments (**Figure S37,** discussed in the later section). Additionally, the ionic hopping mechanism across the pores becomes more evident when a control experiment replaces non-coordinating anions with coordinating anions (NO_3^-), forming a coordination bond with Ag in $MCPNO_3$ for ionic measurement. Such modifications exhibit the ionic conductivity reduction by three orders of magnitude compared to the $MCPSbF_6$.

Next, we aimed to understand the atomistic origin behind the higher electronic conductivity of PF_6-based MOFs compared to the SbF_6-based MOFs from the ground-state electronic structure. All the MOFs exhibit spin unpolarized electronic ground state, confirming the nonmagnetic nature of Ag(I) atoms at the metal nodes. The projected density of states (PDOS) for MCPXF6 MOFs exhibit finite bandgaps (**Figure 4c-d**). Around the Fermi level, the valence band maximum (VBM) in both systems is dominated by the 4d electrons of Ag atoms (contribution = 58%) and 2p electrons of N (contribution = 23.7%) atoms. The charge densities also reveal a predominant distribution of the DOS on the Ag atoms and AgN_3 clusters, as depicted in **Figure S35a-b**. However, the bandgap and the atomic contributions to the CBM state differ significantly with XF_6^- moieties in these MOFs. The CBM of $MCPPF_6$ is dominantly delocalized over C (54%) and N (22.5%) atoms within the MCP unit. Meanwhile, the SbF_6^- units mainly contribute to the CBM state of $MCPSbF_6$. We find that SbF_6^- units incorporate localized molecular states (red-shaded region) just below the electronic states that are delocalized (yellow-shaded) over the organic framework (**Figure 4d**). The presence of such molecular states due to SbF_6^- induces localized states, which ultimately results in less electronic conduction. The electronic structures of $ACPPF_6$ and $ACPSbF_6$ MOFs also show similar results as MCP-based ones, as shown in **Figure S36a-S36d**. Note that the computationally calculated bandgaps are substantially underestimated here due to the use of semi-local exchange-correlation functions during electronic structure simulations.

As a final application, the voltage-controlled hysteretic behavior is utilized to obtain memory devices with $MCPSbF_6$. Note that $MCPSbF_6$ exhibits the highest ionic conductivity and significant hysteresis. Such applications require multiple cycles of biasing of the device; therefore, before starting actual memory measurements, we have performed detailed structural characterization of the $MCPSbF_6$ devices upon multiple cycles of I-V characterization over ± 100 V sweeping. The X-ray diffraction patterns indicate no significant structural variation upon 20 cycles of I-V scan, indicating the overall

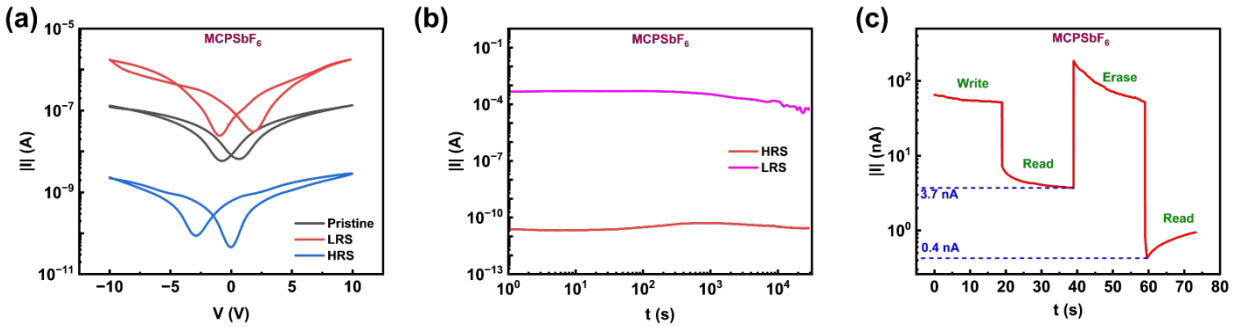

Figure 5. a) I-V characteristics of the memory device fabricated from $MCPSbF_6$ lateral devices (L = 100 µm, W = 1mm) in pristine, LRS and HRS state. For the LRS state, the device was programmed with + 40V (t_{pg} = 5 minutes), and the HRS state was obtained using a programming voltage of - 40V (t_{pg} = 20 minutes). Note that the measurements are performed at a scan rate of 50 V/s. **b)** Time evolution of LRS and HRS states exhibiting retention of the distinct states for more than10^4 seconds. The memristor was configured to a nonvolatile memory state with a t_{pg} = 300 seconds for LRS and 600 seconds for HRS, the E_{pg} = ± 0.4 V/µm and the channel current was monitored using a voltage of – 2.5 V. **c)** Write-Read-Erase-Read (WRER) cycle: I-t characteristics showing LRS to HRS switching. Voltages were given in the sequence: write at 40 V for 20s → read at -2.5 V → erase at -80 V for 20s → read at -2.5 V.

stability of the device towards any bias-induced damage (**Figure S37**). Note that for the majority of measurements, we utilize less than 20 cycles, which indicates the robustness of the device and its measurements. Similarly, detailed microscopic characterization of the device also exhibits stability of the device towards multiple cycles of biasing, indicating the inherent stability (**Figure S38)**. We are able to perform the resistive switching in lateral two-terminal devices fabricated with $MCPSbF_6$. Unlike conventional resistive switching devices, which rely on the electroforming process, here, the ionic migration under bias modulates the resistance of the channel. This resistive switching behavior is utilized to demonstrate memory application. Discrete non-volatile LRS and HRS states were probed by programming the device with an electric field of ±0.4V/µm. This variation of the I-V characteristics upon programming is depicted in **Figure 5a**. Note that the scan rate used in this measurement is in the range of 50 – 200 V/s. I-V measurement indicates that positive field programming results in a low resistance state (LRS or SET) and negative field results in a High resistance state (HRS or RESET), both of which are indicated by a clear vertical shift in the I-V characteristics by 10^3 – 10^4 orders of current (**Figure 5a**). Note that we observe a non-zero current value at 0V bias. This behaviour is majorly attributed to the redistribution of ions across the channel due to the measurement process, which involves higher biasing in the initial condition. This ionic migration results in an inherent potential in the channel, giving rise to a small current whose magnitude depends on the extent of ion migration. Moreover, in order to realize LRS and HRS, we pre-pole the devices, which further creates redistribution of ions and non-zero current value at 0 V. The device was further examined for the reconfigurability of non-volatile and volatile states of memory. In order to drive the device to a non-volatile memory regime, the LRS state is achieved by applying a field of +0. 4V/µm for 300 seconds and the evolution of the channel current was probed at V = - 2.5 V for more than 10^4 Seconds (**Figure 5b**). We observed that the channel current remains fairly constant over the complete duration of the measurement. Similarly, the device was programmed to HRS by applying a field of -0.4V/µm for 20 min, and the channel current was monitored at - 2.5 V. Notably, even the HRS remains fairly constant throughout the complete measurement time, and the ratio of the channel current between LRS and HRS was retained in the range of 10^6 – 10^7 for 10^4 seconds. From the time evolution of the LRS and HRS, we have fitted a power law using the expression: $y = a + bx^v$. The power law exponent was found to be as low as 0.04 for the HRS and

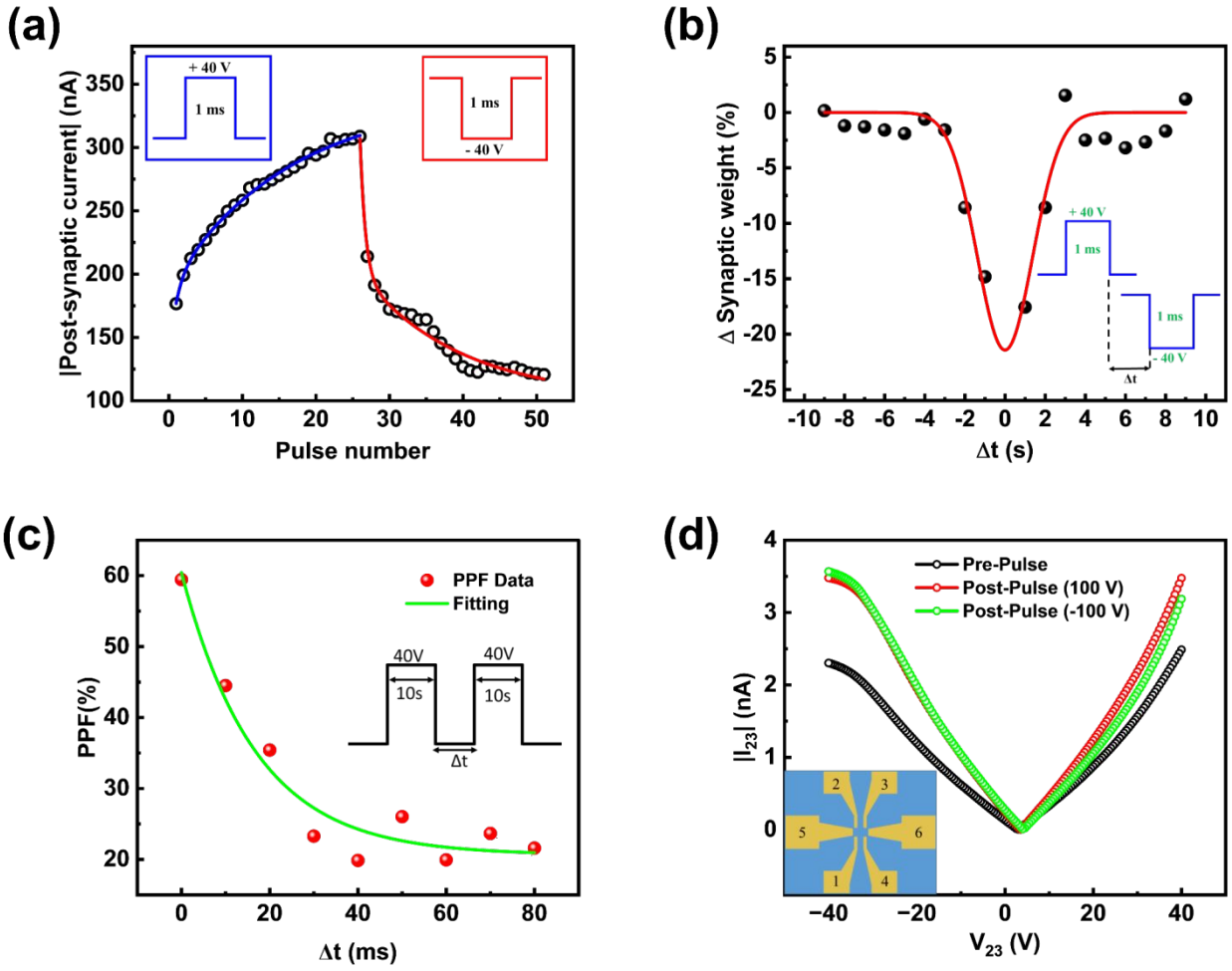

Figure 6. a) Post-synaptic current variation with pulse number, showing Long long-term potentiation (LTP) and Long-Term Depression (LDP) of $MCPSbF_6$ memory device (L = 100 µm, W = 1mm) under successive stimulation using 40 V and - 40 V pulses of 1 ms pulse width while reading at -2.5 V. **b)** Implementation of Spike-Timing-Dependent-Plasticity (STDP) in $MCPSbF_6$ memory device (L = 100 µm, W = 1mm) exhibiting symmetric anti-Hebbian learning. The solid line is a Gaussian fit with a time constant of 1.37 ms. **c)** Demonstration of Paired Pulse Facilitation performed on the same device. The fit was performed with $y = y_0 + A*\exp(R_0*x)$, with $R_0 = -0.06$ ms^{-1} **d)** $|I_{23}|$ versus V_{23} curve before and after applying 100 V & -100 V pulse of 5s duration between terminal 5 and 6 (inset shows the schematic of the device structure), representing the heterosynaptic plasticity property. Inset **Figure 6a-c** depicts the input programming pulses.

a value of 0.03 to 0.1 for the LRS. This time evolution, when extrapolated, results in a retention time of up to 10^{10} – 10^{13} seconds, which corresponds to a time scale of 100 - 1000 years. Further, the reconfigurability of the device for the volatile operation was examined by performing a WRER(Write-Read-Erase-Read) and endurance measurements (**Figure 5c, S39**). For the WRER cycle, the devices were programmed with a writing voltage of + 40V; however, for a lesser time of only 20s and for the erase voltage, a programming voltage of -80V for 20s was applied, and the channel current was monitored at - 2.5V. In this way, we were able to switch the device to LRS and HRS with an I_{ON}/I_{OFF} ratio of ~10, which is reasonable considering this conduction mechanism in this class of ionic solids.[7, 25] Notably, in all the memory measurements, a maximum programming field (E_{pg}) ~ 0.4 – 0.8 V/µm is utilized, which corresponds to a maximum voltage of 16 V if a 20 µm channel is utilized. Nevertheless, this magnitude of current allowed us to operate our devices with low energy consumption at values comparable to other state-of-the-art neuronal circuits. Notably, the energy requirement for the reading operation is as low as ~ 9 nJ, whereas the writing operation requires around 22.8 µJ of energy. We then characterized the endurance of these memory devices by switching the device multiple times to the LRS and HRS states. These devices can be switched for more than 175 cycles, during which LRS and HRS states of conduction can be distinctly identified (**Figure S39**). This level of device performance was also realized on a flexible device.

As a next step, we explore the possibility of designing neural circuits using the two-terminal memory device fabricated from $MCPSbF_6$. These resistive switchable memory devices exhibit synaptic functions like Long-Term Potentiation (LTP) and Long-Term Depression (LTD) of neurons (**Figure 6a**) with repetitive positive and negative bias pulses of 1 ms duration. The resulting time constant of this process is observed to be in the range of 5–7 ms, which is comparable to the response time of biological synapses.[3, 72] Repetitive stimulation by programming pulses of 0.4V/µm and 1 ms duration as the pre-synaptic pulse increases the post-synaptic current by 88% over 25 pulses, gradually bringing the device to LRS consistent with cognitive learning. Similarly, with a - 0.4V/µm pulse of 1ms pulse-width, the post-synaptic current decreases by 66% over 25 pulses. Upon measurement of the change in synaptic weight as a function of the time delay between pre-synaptic and post-synaptic pulses, it was observed that $MCPSbF_6$ memory devices exhibit a Spike-Timing-Dependent-Plasticity (STDP) with symmetric anti-Hebbian learning (**Figure 6b**) which is an important attribute of the spiking neural networks (SNN). By fitting the curve with the Gaussian function, the time constant was found to be 1.37 ms, comparable to the response times of biological synapses, thereby indicating that our memory device emulates neuronal learning.[73] We observe that in our devices, it is possible to obtain synaptic responses and learning with a power consumption of 1 nJ. The second most important indicator of SNN is Paired Pulse Facilitation (PPF). The excitatory post-synaptic current is significantly enhanced by the stimulation with action potential by up to 60 % (**Figure 6c),** indicating the easier configurability of our memory device with increased neurotransmitter release probability, which surpasses the PPF index observed in the majority of MOF-based neuromorphic devices reported till date (**Table S4**). Since the synapses in the brain outnumber neurons significantly, hence multi-terminal mersisters are essential to demonstrate more complex brain operations such as heterosynaptic plasticity.[74] A six-terminal device was used to showcase heterosynaptic plasticity and replicate the functioning of multiple synaptic connections in neurons (shown in the inset of **Figure 6d**). The experiment involved applying field pulses of ±1V/µm of 5 seconds pulse width between the outer electrodes (5&6) of the device, which were not directly connected to the inner electrodes (2&3). This voltage modulation resulted in the alternation of conductance between the inner electrodes, effectively mimicking the behavior of multiple synaptic connections (**Figure 6d** and **S40**). In this case, the energy consumption per synapse is estimated to be between 16 nJ - 23 nJ (Detailed calculations to estimate energy consumption have been provided in **SI section 13.2**). Notably, despite the low switching ratio, the possibility of multi-terminal neuromorphism is a significant step towards neuronal computing with this class of materials, which follow an ionic learning response like biological synapses.

Conclusions

In summary, we have synthesized a group of solution-processable MOFs consisting of Ag(I) dimers coordinated with tridentate N7-alkyl-purine derivatives. Through a combination of structural characterization, electrical measurements, and atomistic simulations, we develop a comprehensive understanding of structure-functionality in this class of materials. Structural characterization indicates the formation of an array of bimetallic centers which provide a conduction channel pathway. Simulation studies indicate that the MOF structure and the electrostatic interaction between the MOF structure and the anion determined the ionic and electronic conductivity, which is consistent with the experimental conductivity. Notably, with the application of a bias voltage, a structural modification to the MOF is observed along with the associated vacancy-induced ionic migration, which results in hysteretic characteristics and memory behavior. Among all MOFs, a two-terminal memristive device fabricated from $MCPSbF_6$ exhibits the most promising result, with a non-volatile memory retention time of more than 10^4 seconds (extrapolated to > 100 years of retention) and an I_{ON}/I_{OFF} ratio of 10^7. Furthermore, owing to the precise control of the level of conductivity in these devices, we reported various functionalities of neurons with a signature of symmetric anti-Hebbian learning with energy consumption in the order of 9 - 20 nJ, comparable to the state-of-the-art neuronal CMOS circuits. Notably, the PPF index and STDP ratio obtained from these devices are among the best in comparison to other MOF-based devices. More importantly, the learning mechanism in these devices is based on the electrical modulation of ionic conductivity through chemically designed porous ionic channels analogous to the mechanism of conduction observed with biological synapses. Our results pave the way for bi-metallic MOFs to develop neurologically inspired electronic functionalities using ionic-based memory mechanisms like synaptic calcium and potassium ion motion.

Methods:

Synthesis of ACP-SbF_6 MOF

Two vials containing 2.5 mL methanol, ACP ligand (10 mg, 0.051 mmol, 3 equiv.), and $AgSbF_6$ salt (11.77 mg, 0.034 mmol, 2 equiv.) were dissolved. $AgSbF_6$ solution was added dropwise to the ACP solution. The solution was kept undisturbed in dark conditions. In three days, Colorless needle-like crystals were obtained. A suitable crystal was chosen from there for single crystal analysis. $ACPSbF_6$ solutions were made by mixing a 1.5 mL methanol solution containing 10 mg of ACP with a 1.5 mL methanol solution containing

11.77 mg $AgSbF_6$. After 1 hour, 100 µL from each solution was collected and utilized to fabricate the device.

Synthesis of MCP-SbF_6 MOF

MCP ligand (10 mg, 0.059 mmol, 1 equiv.) solution and $AgSbF_6$ salt (20.383 mg, 0.059 mmol, 1 equiv.) solution were prepared in 2.5 mL methanol in separate vials. Slowly, $AgSbF_6$ solution was added dropwise to the MCP ligand solution and left undisturbed in the dark. Colourless block crystals suitable for single crystal study were formed in 2 days. $MCPSbF_6$ solutions were made by mixing a 1.5 mL methanol solution containing 10 mg of MCP with a 1.5 mL methanol solution containing 20.38 mg $AgSbF_6$. After 2 hours, 100 µL from each solution was collected and utilized to fabricate the device.

A similar procedure was followed for the synthesis of $ACPPF_6$ and $MCPPF_6$ MOFs. The details are in the supporting information.

Device Fabrication:

To estimate the charge transport characteristics of these molecules, two-terminal lateral devices were fabricated using Cr/Au electrodes on precleaned glass substrates. 4 nm of Cr followed by 21 nm of Au were deposited (using Moorfield MiniLab 026 thermal evaporator) at the rate of 0.5 Å/s to fabricate lateral devices of 100 µm channel length. The substrates were then exposed to UV-Ozone for 15 min to improve the surface wettability. 100 µl of the individual molecules (20 mM concentration in methanol for MCP-based metallopolymers and 11.5 mM concentration in methanol for ACP-based metallopolymers) were drop cast on the substrates, and the films were then dried in two ways (A detailed step by step fabrication procedure is provided in supplementary **Section 3**). The first method is drying in a dark environment at room temperature for 30 minutes, and the second is annealing at 80 °C for 15 minutes. Different channel lengths were patterned on glass substrates using Heidelberg µMLA Maskless Aligner to investigate channel length-dependent charge transport properties. For performing the heterosynaptic plasticity measurement of the $MCPSbF_6$ MOF, a six-terminal device similar to a Hall bar geometry was fabricated with Cr/Au electrodes on a 1.5 × 1.5 cm glass substrate using photolithography with a standard photomask.

Device Characterization:

All the electrical characterizations were performed at room temperature and atmospheric pressure in a Lake Shore CRX-6.5K Cryogenic Probe Station integrated with Keysight B1500A semiconductor parameter analyzer and home-built LabVIEW programs.

Scan rate-dependent I-V measurement: The scan rate of an I-V sweep is estimated by dividing the voltage step size by the sum of integration time and delay time. Scan rate-dependent I-V measurements were taken by setting different values of integration time and delay time in the B1500A semiconductor parameter analyzer (**Table S2**). The scan rate varied from 4 V/s to 500 V/s while maintaining the voltage step size fixed at 2 V for these measurements.

***Ionic conductivity measurement*:** The combined conductivity of electrons and ions was estimated by applying Ohm's law on I-V characteristics taken at a higher scan rate (10000 V/s) such that there is no hysteresis. A constant current of 20 pA - 2 nA was applied to the device to measure the electronic conductivity using a galvanostatic measurement. The electronic conductivity is calculated from the saturation regime in the time evolution of the resistance curve where there is no ionic movement. The ionic conductivity is then determined by subtracting the electronic conductivity from the total conductivity.

***Memory measurements*:** Memory measurements were performed using Keysight B1500A semiconductor parameter analyzer with home-built LabVIEW programs. The device was taken to LRS state by applying + 40V for 300 s and HRS state by - 40V for 600 s. Both the states were monitored for more than 10^4 seconds using a bias voltage of - 2.5V. The volatile WRER memory cycles were performed in the following way: write or LRS is obtained by poling the device at + 40 V, 20 s, erase or HRS at – 80 V, 20s, and the channel current was read at – 2.5 V in both the cases. Endurance measurements were performed by taking the device to LRS and HRS alternatively by poling them at +10 V, 10 s for LRS and -20 V, 10 s for HRS time and probing the current in each state at -2.5V for more than 200 cycles; we were able to identify the two states distinctly for up to 175 cycles.

***Neuromorphic measurements*:** By increasing the number of applied pre-synaptic pulses of + 40V (pulse width = 1 ms) and then post-synaptic pulses of - 40V (pulse width = 1 ms), Long Term Potentiation (LTP) and Long-Term Depression (LDP) were observed. Spike time-dependent plasticity was obtained from the time difference between pre and post-synaptic pulse from -10 ms to 10 ms. PPF data were obtained by applying two consecutive pulses of + 40V separated by a varying time duration ranging from 0 ms to 80 ms. In the case of heterosynaptic plasticity, the current change across two inner electrodes was observed after applying 100 V and -100 V for 5s across the outer electrodes.

Author Contributions

C.S.P. and SPS conceived the project directions and experiments. SJP and KRK contributed equally to the work. S.J.P. synthesized the MOFs and carried out crystallization. S.J.P. and S.K.A carried out all the physical characterization under the supervision of C.S.P. KRK, S.N., and S.K.P. fabricated the device and carried out all the memory and neuromorphic study under the supervision of S.P.S. D.P., and P.D carried out all the computational work under the supervision of D.G. C.S.P. and S.P.S. equally supervised the overall project. The manuscript was Finalized by C.S.P and S.P.S. with input from all authors

Data availability

[CCDC 2264862-2264865 contains the supplementary crystallographic data for this paper. These data can be obtained free of charge from The Cambridge Crystallographic Data Centre via www.ccdc.cam.ac.uk/data_request/cif.]

Supporting Information

Supporting Information is available online.

Acknowledgments

SJP and SKA gratefully acknowledge DAE for providing Senior Research Fellowship in Ph.D. SKP and SN thank DAE, the Government of India, for financial support through the DISHA scholarship. SPS acknowledges funding support from the Royal Society through the Newton Alumni Fellowship (AL/211004, AL/201019, and AL/191021), Science and Engineering Research Board (SERB-SRG/2020/001641

and IPA/2021/000096). CSP and SPS acknowledge funding from the Department of Atomic Energy (DAE, RIN-4001, RIN-4002), Government of India. DG acknowledges the IIT Delhi SEED Grant (PLN12/04MS), the Science and Engineering Research Board (SERB), Department of Science and Technology (DST), India for Start-up Research Grant SRG/2022/00l234 and the IIT Delhi HPC facility for computational resources. This work was performed, in part, at the Center for Integrated Nanotechnologies, an Office of Science User Facility operated for the U.S. Department of Energy (DOE) Office of Science by Los Alamos National Laboratory (Contract 89233218CNA000001) and Sandia National Laboratories (Contract DE-NA-0003525).

Conflicts of interest

There are no conflicts to declare.

Additional information

Supplementary information

The online version contains supplementary material available at

Correspondence and requests for materials should be addressed to purohit@niser.ac.in, satyaprasad@niser.ac.in,dibyajyoti@iitd.ac.in

References

1. S. Bianchi, I. Muñoz-Martin, E. Covi, A. Bricalli, G. Piccolboni, A. Regev, G. Molas, J. F. Nodin, F. Andrieu and D. Ielmini, *Nat. Commun.*, 2023, **14**, 1565.
2. D. Marković, A. Mizrahi, D. Querlioz and J. Grollier, *Nat. Rev. Phys*, 2020, **2**, 499-510.
3. V. K. Sangwan, H.-S. Lee, H. Bergeron, I. Balla, M. E. Beck, K.-S. Chen and M. C. Hersam, *Nature*, 2018, **554**, 500-504.
4. M. A. Zidan, J. P. Strachan and W. D. Lu, *Nat. Electron.*, 2018, **1**, 22-29.
5. T. Hasegawa, K. Terabe, T. Tsuruoka and M. Aono, *Adv. Mater.*, 2012, **24**, 252-267.
6. S. Kumar, X. Wang, J. P. Strachan, Y. Yang and W. D. Lu, *Nat. Rev. Mater.*, 2022, **7**, 575-591.
7. R. Waser, R. Dittmann, G. Staikov and K. Szot, *Adv. Mater.*, 2009, **21**, 2632-2663.
8. Y. Kim, A. Chortos, W. Xu, Y. Liu, J. Y. Oh, D. Son, J. Kang, A. M. Foudeh, C. Zhu, Y. Lee, S. Niu, J. Liu, R. Pfattner, Z. Bao and T.-W. Lee, *Science*, 2018, **360**, 998-1003.
9. M. Wang, J. Tu, Z. Huang, T. Wang, Z. Liu, F. Zhang, W. Li, K. He, L. Pan, X. Zhang, X. Feng, Q. Liu, M. Liu and X. Chen, *Adv. Mater.*, 2022, **34**, 2201962.
10. Y.-X. Hou, Y. Li, Z.-C. Zhang, J.-Q. Li, D.-H. Qi, X.-D. Chen, J.-J. Wang, B.-W. Yao, M.-X. Yu, T.-B. Lu and J. Zhang, *ACS Nano*, 2021, **15**, 1497-1508.
11. S. M. Kwon, S. W. Cho, M. Kim, J. S. Heo, Y.-H. Kim and S. K. Park, *Adv. Mater.*, 2019, **31**, 1906433.
12. Q.-B. Zhu, B. Li, D.-D. Yang, C. Liu, S. Feng, M.-L. Chen, Y. Sun, Y.-N. Tian, X. Su, X.-M. Wang, S. Qiu, Q.-W. Li, X.-M. Li, H.-B. Zeng, H.-M. Cheng and D.-M. Sun, *Nat. Commun.*, 2021, **12**, 1798.
13. J.-K. Han, M. Kang, J. Jeong, I. Cho, J.-M. Yu, K.-J. Yoon, I. Park and Y.-K. Choi, *Adv. Sci*, 2022, **9**, 2106017.
14. Y. Zhang, E. R. W. van Doremaele, G. Ye, T. Stevens, J. Song, R. C. Chiechi and Y. van de Burgt, *Adv. Mater.*, 2022, **34**, 2200393.
15. S. G. Sarwat, T. Moraitis, C. D. Wright and H. Bhaskaran, *Nat. Commun.*, 2022, **13**, 2247.
16. Q. Chen, X. Zhang, Y. Liu, Y. Yan, R. Yu, X. Wang, Z. Lin, H. Zeng, L. Liu, H. Chen and T. Guo, *Nano Energy*, 2022, **94**, 106931.
17. S. T. Keene, A. Melianas, Y. van de Burgt and A. Salleo, *Adv. Elect. Mat.*, 2019, **5**, 1800686.
18. C. Lubrano, U. Bruno, C. Ausilio and F. Santoro, *Adv. Mater.*, 2022, **34**, 2110194.
19. J. Ouyang, C.-W. Chu, C. R. Szmanda, L. Ma and Y. Yang, *Nat. Mater*, 2004, **3**, 918-922.
20. J. C. Scott and L. D. Bozano, *Adv. Mater.*, 2007, **19**, 1452-1463.
21. S. Song, B. Cho, T.-W. Kim, Y. Ji, M. Jo, G. Wang, M. Choe, Y. H. Kahng, H. Hwang and T. Lee, *Adv. Mater.*, 2010, **22**, 5048-5052.
22. H. Wang, F. Meng, B. Zhu, W. R. Leow, Y. Liu and X. Chen, *Adv. Mater.*, 2015, **27**, 7670-7676.
23. Y. Yang, J. Ouyang, L. Ma, R. J.-H. Tseng and C.-W. Chu, *Adv. Funct. Mater.*, 2006, **16**, 1001-1014.
24. Z. Zhao, M. E. El-Khouly, Q. Che, F. Sun, B. Zhang, H. He and Y. Chen, *Angew. Chem. Int. Ed.*, 2023, **62**, e202217249.
25. D. Kuzum, S. Yu and H. S. Philip Wong, *Nanotechnology*, 2013, **24**, 382001.
26. R. A. Kharod, J. L. Andrews and M. Dincă, *Annu. Rev. Mater. Res.*, 2022, **52**, 103-128.
27. L. Sun, M. G. Campbell and M. Dincă, *Angew. Chem. Int. Ed.*, 2016, **55**, 3566-3579.
28. L. S. Xie, G. Skorupskii and M. Dincă, *Chem. Rev.*, 2020, **120**, 8536-8580.
29. M. Zhang, C. Ma, D. Du, J. Xiang, S. Yao, E. Hu, S. Liu, Y. Tong, W.-Y. Wong and Q. Zhao, *Adv. Elect. Mat.*, 2020, **6**, 2000841.
30. J. Liu, F. Yang, L. Cao, B. Li, K. Yuan, S. Lei and W. Hu, *Adv. Mater.*, 2019, **31**, 1902264.
31. S. Chen, Y. Ju, Y. Yang, F. Xiang, Z. Yao, H. Zhang, Y. Li, Y. Zhang, S. Xiang, B. Chen and Z. Zhang, *Nat. Commun.*, 2024, **15**, 298.
32. L. G. S. Albano, T. P. Vello, D. H. S. de Camargo, R. M. L. da Silva, A. C. M. Padilha, A. Fazzio and C. C. B. Bufon, *Nano Lett.*, 2020, **20**, 1080-1088.
33. Z. Yao, L. Pan, L. Liu, J. Zhang, Q. Lin, Y. Ye, Z. Zhang, S. Xiang and B. Chen, *Sci. Adv.*, 2019, **5**, eaaw4515.
34. J. K. Bera and K. R. Dunbar, *Angew. Chem. Int. Ed.*, 2002, **41**, 4453-4457.
35. J. F. Berry, in *Metal-Metal Bonding*, ed. G. Parkin, Springer Berlin Heidelberg, Berlin, Heidelberg, 2010, DOI: 10.1007/978-3-642-05243-9_1, pp. 1-28.
36. C. H. Hendon, A. Walsh, N. Akiyama, Y. Konno, T. Kajiwara, T. Ito, H. Kitagawa and K. Sakai, *Nat. Commun.*, 2016, **7**, 11950.
37. R. H. Ismayilov, W.-Z. Wang, G.-H. Lee, C.-Y. Yeh, S.-A. Hua, Y. Song, M.-M. Rohmer, M. Bénard and S.-M. Peng, *Angew. Chem. Int. Ed.*, 2011, **50**, 2045-2048.
38. K. Krogmann, *Angew. Chem. Int. Ed.*, 1969, **8**, 35-42.
39. K. Tanaka, A. Tengeiji, T. Kato, N. Toyama and M. Shionoya, *Science*, 2003, **299**, 1212-1213.
40. G. R. Whittell, M. D. Hager, U. S. Schubert and I. Manners, *Nat. Mater*, 2011, **10**, 176-188.

41. I.-W. P. Chen, M.-D. Fu, W.-H. Tseng, J.-Y. Yu, S.-H. Wu, C.-J. Ku, C.-h. Chen and S.-M. Peng, *Angew. Chem. Int. Ed.*, 2006, **45**, 5814-5818.
42. G. Givaja, P. Amo-Ochoa, C. J. Gómez-García and F. Zamora, *Chem. Soc. Rev.*, 2012, **41**, 115-147.
43. I.-W. P. Chen, M.-D. Fu, W.-H. Tseng, J.-Y. Yu, S.-H. Wu, C.-J. Ku, C.-h. Chen and S.-M. Peng, *Angew. Chem. Int. Ed.*, 2006, **45**, 5814-5818.
44. J. L. Greenfield, D. Di Nuzzo, E. W. Evans, S. P. Senanayak, S. Schott, J. T. Deacon, A. Peugeot, W. K. Myers, H. Sirringhaus, R. H. Friend and J. R. Nitschke, *Adv. Mater.*, 2021, **33**, 2100403.
45. H. Wang, J. Yang, Z. Wang, Y. Shao, Y. Tang, J. Guo and X. Yan, *Applied Physics Reviews*, 2024, **11**.
46. X. Yan, X. Jia, Y. Zhang, S. Shi, L. Wang, Y. Shao, Y. Sun, S. Sun, Z. Zhao, J. Zhao, J. Sun, Z. Guo, Z. Guan, Z. Zhang, X. Han and J. Chen, *Nano Energy*, 2023, **107**, 108091.
47. S. Sivakova and S. J. Rowan, *Chem. Soc. Rev.*, 2005, **34**, 9-21.
48. S. Verma, A. K. Mishra and J. Kumar, *Acc. Chem. Res.*, 2010, **43**, 79-91.
49. S. J. Panda, S. K. Agrawalla and C. S. Purohit, *CrystEngComm*, 2024, **26**, 4418-4430.
50. J. M. González-Pérez, C. Alarcón-Payer, A. Castiñeiras, T. Pivetta, L. Lezama, D. Choquesillo-Lazarte, G. Crisponi and J. Niclós-Gutiérrez, *Inorg. Chem.*, 2006, **45**, 877-882.
51. M. Köberl, M. Cokoja, W. A. Herrmann and F. E. Kühn, *Dalton Trans.*, 2011, **40**, 6834-6859.
52. J. Thomas-Gipson, G. Beobide, O. Castillo, M. Fröba, F. Hoffmann, A. Luque, S. Pérez-Yáñez and P. Román, *Cryst. Growth Des.*, 2014, **14**, 4019-4029.
53. S. Jyoti Panda, S. Kumar Agrawalla and C. Shekhar Purohit, *Chemistry – An Asian Journal*, **n/a**, e202400985.
54. V. F. Yusuf, N. I. Malek and S. K. Kailasa, *ACS Omega*, 2022, **7**, 44507-44531.
55. S. Chen, R. F. Graceffa and A. A. Boezio, *Org. Lett.*, 2016, **18**, 16-19.
56. G. Teja Illa, P. Satha and C. S. Purohit, *CrystEngComm*, 2016, **18**, 5512-5518.
57. C. S. Purohit and S. Verma, *J. Am. Chem. Soc.*, 2006, **128**, 400-401.
58. C. S. Purohit and S. Verma, *J. Am. Chem. Soc.*, 2007, **129**, 3488-3489.
59. according, *to CCDC version 2023.1.0*.
60. L. P. Olson, D. R. Whitcomb, M. Rajeswaran, T. N. Blanton and B. J. Stwertka, *Chem. Mater.*, 2006, **18**, 1667-1674.
61. M. A. Carvajal, J. J. Novoa and S. Alvarez, *J. Am. Chem. Soc.*, 2004, **126**, 1465-1477.
62. C. Xu, C. Li and Y. Jin, *Small*, 2020, **16**, e2002727.
63. M. J. Lee, S.-H. Kim, S. Lee, C. Yoon, K.-A. Min, H. Choi, S. Hong, S. Lee, J.-G. Park, J.-P. Ahn and B. H. Park, *NPG Asia Mater.*, 2020, **12**, 82.
64. M. Schalenbach, B. Hecker, B. Schmid, Y. E. Durmus, H. Tempel, H. Kungl and R.-A. Eichel, *Electrochem. Sci. Adv.*, 2023, **3**, e2100189.
65. G. Richardson, S. E. J. O'Kane, R. G. Niemann, T. A. Peltola, J. M. Foster, P. J. Cameron and A. B. Walker, *Energy Environ. Sci.*, 2016, **9**, 1476-1485.
66. S. P. Senanayak, M. Abdi-Jalebi, V. S. Kamboj, R. Carey, R. Shivanna, T. Tian, G. Schweicher, J. Wang, N. Giesbrecht, D. Di Nuzzo, H. E. Beere, P. Docampo, D. A. Ritchie, D. Fairen-Jimenez, R. H. Friend and H. Sirringhaus, *Sci. Adv.*, 2020, **6**, eaaz4948.
67. S. K. Patel, S. Nayak and S. P. Senanayak, *ACS Appl. Electron. Mater.*, 2023, DOI: 10.1021/acsaelm.3c00393.
68. Y.-C. Zhao, W.-K. Zhou, X. Zhou, K.-H. Liu, D.-P. Yu and Q. Zhao, *Light Sci. Appl.*, 2017, **6**, e16243-e16243.
69. N. Niharika Bhuyan, S. Shankar S, S. Jyoti Panda, C. Shekhar Purohit, R. Singhal, G. D. Sharma and A. Mishra, *Angew. Chem. Int. Ed.*, 2024, **n/a**, e202406272.
70. I. Hussain, M. Z. Ansari, M. Ahmad, A. Ali, T. Nawaz, T. Hussain, C. Lamiel, M. Sufyan Javed, X. Chen, M. Sajjad, T. Kaewmaraya, K. Khan and K. Zhang, *Adv. Funct. Mater.*, 2023, **33**, 2302888.
71. V. Ásgeirsson, B. O. Birgisson, R. Bjornsson, U. Becker, F. Neese, C. Riplinger and H. Jónsson, *Journal of Chemical Theory and Computation*, 2021, **17**, 4929-4945.
72. Q. Lu, F. Sun, L. Liu, L. Li, Y. Wang, M. Hao, Z. Wang, S. Wang and T. Zhang, *Microsyst. Nanoeng.*, 2020, **6**, 84.
73. R. S. Zucker and W. G. Regehr, *Annu Rev Physiol*, 2002, **64**, 355-405.
74. S. Kim, C. Du, P. Sheridan, W. Ma, S. Choi and W. D. Lu, *Nano Lett.*, 2015, **15**, 2203-2211.

Table of Content

This research showcases the development and application of bioinspired MOFs in neuromorphic devices. These MOFs possess accessible porous channels, enabling ions to move under voltage bias. Being solution processable, they can be seamlessly integrated into devices, emulating multi-terminal complex synaptic responses.